Visualization and structural analysis of the bacterial magnetic organelle magnetosome using atomic force microscopy

Daisuke Yamamoto[a,b,1], Azuma Taoka[c,1], Takayuki Uchihashi[a,b], Hideaki Sasaki[c], Hiroki Watanabe[a], Toshio Ando[a,b,d], and Yoshihiro Fukumori[c,2]

[a]Department of Physics, Kanazawa University, Kakuma-machi, Kanazawa 920-1192, Japan; [b]Core Research for Evolutional Science and Technology, Japan Science and Technology Agency, Sanban-cho, Chiyoda-ku, Tokyo 102-0075, Japan; [c]Department of Life Science, Graduate School of Natural Science and Technology, Kanazawa University, Kakuma-machi, Kanazawa 920-1192, Japan; and [d]Frontier Science Organization, Kanazawa University, Kakuma-machi, Kanazawa 920-1192, Japan

Edited by Dianne K. Newman, Caltech/ Howard Hughes Medical Institute, Pasadena, CA, and accepted by the Editorial Board April 8, 2010 (received for review February 16, 2010)

The unique ability of magnetotactic bacteria to navigate along a geomagnetic field is accomplished with the help of prokaryotic organelles, magnetosomes. The magnetosomes have well-ordered chain-like structures, comprising membrane-enveloped, nano-sized magnetic crystals, and various types of specifically associated proteins. In this study, we applied atomic force microscopy (AFM) to investigate the spatial configuration of isolated magnetosomes from *Magnetospirillum magneticum* AMB-1 in near-native buffer conditions. AFM observation revealed organic material with a ~7-nm thickness surrounding a magnetite crystal. Small globular proteins, identified as magnetosome-associated protein MamA, were distributed on the mica surface around the magnetosome. Immuno-labeling with AFM showed that MamA is located on the magnetosome surface. In vitro experiments showed that MamA proteins interact with each other and form a high molecular mass complex. These findings suggest that magnetosomes are covered with MamA oligomers in near-native environments. Furthermore, nanodissection revealed that magnetosomes are built with heterogeneous structures that comprise the organic layer. This study provides important clues to the supramolecular architecture of the bacterial organelle, the magnetosome, and insight into the function of the proteins localized in the organelle.

magnetotactic bacteria | scanning probe microscopy | nanoparticle | TPR protein | protein localization

Magnetosomes are unique prokaryotic organelles synthesized in magnetotactic bacteria, which function as a cellular compass to navigate along the Earth's magnetic field (1–4). Proteomic analyses of the isolated magnetosomes indicate that the magnetosome contains various types of specific associated proteins (5–7). Most of the magnetosome-associated proteins are encoded in gene clusters within a genetic "magnetosome island," which is essential for the synthesis of magnetosomes (8–11). These proteins are thought to function in magnetite biomineralization, magnetic sensing, formation of the magnetosome vesicle, and construction of magnetosomal structures.

Insights into the magnetosome structure were provided using transmission electron microscopic (TEM) techniques such as negative staining, freeze-etching, and cryo-electron microscopy (12–17). These studies demonstrated that magnetosomes are highly ordered structures. Magnetosomes comprise a chain of regular-sized bio-mineralized magnetite crystals, each of which is surrounded by a lipid bilayer membrane and organic components. Also, individual magnetosome particles are connected by interparticle structures. Furthermore, most magnetosomes are arranged intimately along novel cytoskeletal filaments as visualized by cryo-electron tomography (14, 15, 18–20).

Although a number of important findings about the magnetosome structure have been provided by TEM, there are some disadvantages associated with TEM techniques. TEM techniques require sample preparation methods such as fixation, staining, dehydration, embedding, and thin sectioning, all of which may potentially damage or alter the native structure of biologic specimens. Cryo-electron microscopy does not have these disadvantages, and allows visualization of cellular structures in a near-native, frozen hydrated states. Using this method, 3- to 4-nm resolution has been achieved for putative cytoskeletal filaments in magnetotactic bacteria (14). However, in most of the precedent studies, extraction of fine geometries is prevented for low electron density materials in a crowded environment, such as membrane-embedded proteins surrounded by lipid molecules. This is probably because of the low electron dose that must be used with frozen hydrated materials, which results in a low signal-to-noise ratio of the projection images (21). As a complementary technique, atomic force microscopy (AFM) has been used to visualize organic samples ranging from single molecules to living cells under physiologic conditions (22–24). In AFM, the surface profile of the sample is imaged by detecting the interaction between the sample and the AFM stylus during the raster scanning of the sample. With this imaging technique, biologic molecules can be visualized with a high signal-to-noise ratio. Remarkably, AFM allows molecular resolution imaging of organelles such as bacterial photosynthetic membranes (25) and disk membranes (26). These AFM studies elucidated the organization of networks of constituent molecules in the native membranes, which has been difficult using other methods.

Of particular importance is the identification of the proteinaceous supramolecular structure of the magnetosome. Because of AFM's ability to visualize biologic specimens in their near-native conditions with a high signal-to-noise ratio, AFM can feasibly be used to visualize the constitutions of submicron-sized bacterial organelles at molecular resolution. Here, we applied AFM to investigate the spatial configuration of magnetosomes from *Magnetospirillum magneticum* AMB-1. AFM observations indicated that the thickness of the organic layer wrapped around the magnetite crystal was ~7 nm, and magnetosome-associated protein MamA was localized at the surface of the organic layer. In vitro experiments revealed that MamA proteins interact with

Author contributions: D.Y., A.T., T.A., and Y.F. designed research; D.Y., A.T., T.U., H.S., and H.W. performed research; D.Y. and A.T. analyzed data; and D.Y., A.T., T.U., T.A., and Y.F. wrote the paper.

The authors declare no conflict of interest.

This article is a PNAS Direct Submission. D.K.N. is a guest editor invited by the Editorial Board.

[1]D.Y. and A.T. contributed equally to this work.

[2]To whom correspondence should be addressed. E-mail: fukumor@kenroku.kanazawa-u.ac.jp.

This article contains supporting information online at www.pnas.org/lookup/suppl/doi:10.1073/pnas.1001870107/-/DCSupplemental.

each other to form a high–molecular-mass complex. Moreover, reconstruction experiment of MamA showed a possibility that MamA may contributes to stabilize the magnetosome chain structure as observed using AFM.

Results

Structure of the Purified Magnetosome. In the present study, hydrophilic bare mica and hydrophobilized mica were served as substrates for AFM observations. These surfaces have different affinities for the magnetosomes and magnetosome-associated proteins, as described below. Thus, we used both substrates depending on the object of interest. Although magnetosomes were observed on both substrates, magnetosomes were more efficiently attached to the hydrophobilized mica surface than the bare mica surface.

Figure 1*A* shows an AFM image of the purified magnetosomes adsorbed on the hydrophobilized mica. The chain-like structure of magnetosomes observed by AFM was consistent with that observed by TEM (16). To estimate the organic layer surrounding the magnetite crystals, the height of the magnetosomes and the size of the magnetite crystals were measured vertically along the magnetosome chains using AFM and TEM, respectively. The height of each magnetosome particle was 60.8 ± 7.1 nm (n = 404), whereas the crystal size of the magnetite was 46.9 ± 6.9 nm (n = 298) in diameter. This finding indicated that the individual magnetite crystal is surrounded with ∼7 nm of an electron permeable layer composed of organic components.

Regular-sized globular particles were found to be dispersed on the bare mica (Fig. 1*B*), whereas these particles were not observed around magnetosomes on the hydrophobilized mica. Removal of the particles could not be achieved by further purification of the magnetosomes. Moreover, the particles were not observed around the magnetosomes when the magnetosomes were chemically cross-linked with glutaraldehyde before deposition onto the bare mica. These results strongly suggest that the particles originated from the magnetosomes. Another architectural feature observed by AFM was a sheet-like structure in the proximity of the magnetosomes (Fig. 1*B*, asterisk). This sheet-like structure was observed on both bare mica and hydrophobilized mica. The thickness of the sheet-like structures was ≈3 nm.

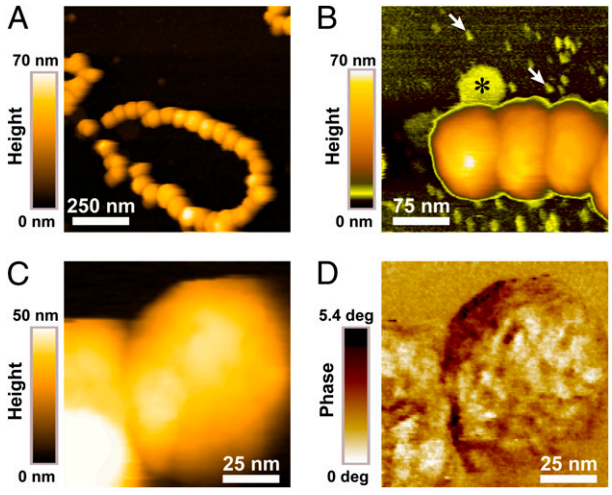

Fig. 1. AFM observations of magnetosomes adsorbed on the mica surfaces. (*A*) AFM image of the magnetosomes chain adsorbed on a hydrophobilized mica surface. (*B*) AFM image of magnetosomes adsorbed on a bare mica surface. Small particles (arrows) and a sheet-like structure (asterisk) were observed in the proximity of the magnetosomes. High-magnification (*C*) topographic and (*D*) phase contrast images of the magnetosome particles on hydrophobilized mica. AFM images were recorded at imaging rates of (*A*) 2.1, (*B*) 1.0, and (*C* and *D*) 4.0 s/frame, and the number of pixels of (*A* and *B*) 256 × 256 and (*C* and *D*) 150 × 150.

The surface of the magnetosome was closely examined by simultaneously obtaining topographic and phase images (Fig. 1 *C* and *D*). In the topographic image, detailed surface structures were difficult to visualize. In contrast, a clear contrast was obtained in the phase image. The phase image showed texture with granular and wrinkled lines on the magnetosome vesicle. The phase contrast of AFM is strongly relevant to several surface properties such as viscoelasticity, elasticity and surface adhesion energy (27). The phase imaging mode allows one to visualize compositional variation, even for the sample that the fine structures are difficult to visualize in the topographic images. Therefore, the phase contrast shown in Fig. 1*D* should represent heterogeneity in the sample, and suggests that the outermost layer of magnetosomes is formed by an amorphous layer of magnetosome-associated proteins.

Identification of Globular Particles Observed on Bare Mica. To understand the origination of the small particles (Fig. 1*B* and Fig. 2*A*), we treated magnetosomes with alkaline buffer. As reported previously, magnetosomal protein MamA (Mam22) and cytochrome cd_1 are efficiently solubilized from magnetosomes by alkaline buffer (13). When the alkaline-treated magnetosomes were loaded onto the bare mica, the small particles were not observed (Fig. 2*B*), whereas a number of particles were observed on the bare mica when the spent alkaline solution was used as a sample (Fig. 2*C*). In contrast, the sheet-like structures were not removed by the alkaline treatment (Fig. S1). Before the alkaline treatment, the height distribution of the particles showed two clear peaks on the histogram (Fig. 2*E*). Most of the particles were ∼3 nm in height, and 6- to 8-nm particles were also detected. The mean height of the particles solubilized from magnetosomes (Fig. 2*F*) was in good agreement with the major distribution of the particles observed before the alkaline treatment.

To identify the small particles, proteins attached to the bare mica were analyzed. A 24-kDa protein band was detected by SDS/PAGE analysis of samples extracted from the mica (Fig. 2*H*), and was positively recognized by anti-MamA antibody (Fig. 2*I*). To further examine the correlation of MamA protein with the globular particles, we observed the purified magnetosomes from the Δ*mamA* mutant of *M. magneticum* AMB-1 (28). In this case, the number density of the particles observed on the bare mica significantly reduced (Fig. 2 *D* and *G*). This clearly indicates that majority of the particles observed around magnetosomes on bare mica are MamA molecules.

In addition to structural imaging, the AFM stylus can be used as a manipulator to dissect individual biologic samples (29, 30). Figure 3 and the supplemental movie show high-speed AFM images of the dissection process of the magnetosomes observed on the bare mica. While the magnetosomes were being imaged, additional tapping force was applied (20–33 frames). The magnetosomes were removed by the scanning stylus. Consequently, sheet-like structures appeared at the initial position of the magnetosome (Fig. 3, asterisks). The appearance and thickness (3 nm) of these sheets were consistent with those of the sheets observed in the proximity of magnetosomes (Fig. 1*B*). These sheets seem to be lipid bilayers, based on their featureless surface structure and thickness that is comparable to the typical value of lipid membranes (3–4 nm) measured by x-ray scattering (31) and AFM (26). Together with the sheet-like structures, additional small particles, which were 3 nm in height, were observed around the magnetosomes after the dissection (Fig. 3, arrowheads). These findings indicated that magnetosomes contain heterogeneous structures that should comprise the organic layer.

Oligomerization of MamA. MamA, one of the most abundant proteins in the magnetosome, contains five or six tetratrico-peptide repeat (TPR) motifs (32, 33) that mediate the protein–protein interactions to assemble the multiprotein complexes (34). There-

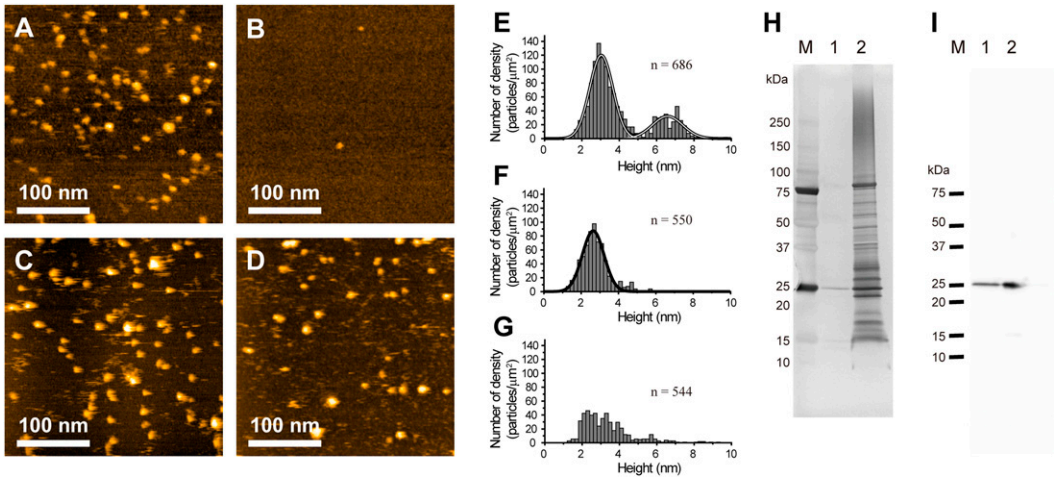

Fig. 2. Identification of small globular proteins found on bare mica. AFM images of small particles observed on bare mica (*A*) before and (*B*) after alkaline treatment of purified magnetosomes. (*C*) AFM micrograph of the particles removed from the purified magnetosomes with alkaline buffer. (*D*) AFM image of particles observed on bare mica around magnetosomes from *ΔmamA* mutant. (*E*) Histogram for heights of small particles observed around the magnetosomes. Black curve represents the fit to the sum of two Gaussians (shown individually in white lines; 3.0 ± 0.6 nm and 6.6 ± 0.8 nm). (*F*) Histogram for heights of the particles removed from magnetosomes by alkaline treatment. Curve represents the fit to a Gaussian distribution (2.6 ± 0.6 nm). (*G*) Histogram for heights of particles observed around magnetosomes from *ΔmamA* mutant. (*H*) Silver-stained SDS/PAGE gel of magnetosomal protein absorbed on bare mica (lane 1), and proteins extracted from the purified magnetosomes (lane 2). Precision Plus protein standard was used (lane M). (*I*) Immunoblot analysis with anti-MamA antibody. The proteins extracted from bare mica and magnetosomes were loaded on lanes 1 and 2, respectively. Magnetosomes were prepared from wild-type *M. magneticum* AMB-1 except for *D* and *G*.

fore, MamA may function as a receptor for the protein–protein interaction in magnetosomes. We examined the partner protein of MamA using *M. magnetotacticum* MS-1. *M. magnetotacticum* MS-1 is very closely related with *M. magneticum* AMB-1. The amino acid sequences of *M. magnetotacticum* MamA ($MamA_{MS-1}$: known as Mam22: BAA11643) and *M. magneticum* AMB-1 MamA ($MamA_{AMB-1}$: known as Mms24: BAE49775) are identical.

For the isolation of MamA-associated proteins, the recombinant N-terminal his-tagged $MamA_{MS-1}$ (His-MamA) was chemically conjugated with the resin to prepare an MamA-affinity column. We subjected solubilized magnetosome-associated proteins from *M. magnetotacticum* MS-1 to the MamA-affinity column. MamA affinity column chromatography showed that one major protein band (23.6 kDa) and four minor protein bands (26.8 kDa, 31.6 kDa, 54.0 kDa, and 63.5 kDa) were eluted (Fig. 4*A*). The 23.6-kDa protein was identified to be $MamA_{MS-1}$ by immunoblotting (Fig. S2). Unfortunately, the N-terminal amino acid sequences of the four minor protein bands were not determined because the amounts of these proteins were not sufficient to analyze. To confirm this result, a pull-down assay was performed. $MamA_{MS-1}$ was coprecipitated with His-MamA (Fig. 4*B*). These results indicated that MamA proteins interact with each other and form an oligomeric complex.

We examined the oligomerization status of the recombinant MamA. Purified His-MamA was separated by gel filtration into a single peak, which was estimated to be 560 kDa (Fig. S3). To further analyze the oligomeric status of His-MamA, we examined the peak fractions of the gel filtration by AFM. On the bare mica, we observed small particles (~3 nm in height), similar to that shown in Fig. 2*A*, instead of a large complex (Fig. S4). In contrast, His-MamA oligomers were visualized on aminosilane-functionalized mica (AP-mica). The AFM image of oligomerized His-MamA revealed a unique configuration: a regular-sized, rugged-shaped globular structure (Fig. 4 *C* and *D*). The size of the observed complex ranged from 4.5 to 6.5 nm in height and 14–20 nm in diameter. This agrees with the molecular mass estimated from the gel filtration column chromatography.

Localization of MamA Protein Complexes in the Magnetosomes. Immuno-labeling was performed to identify the location of $MamA_{AMB-1}$ in the magnetosomes using AFM. Figure 5*A* shows an AFM image of the magnetosomes labeled with anti-MamA antibodies. After labeling, antibodies bound densely to magnetosomes. By contrast, preimmune serum, which has no significant affinity for MamA, had no effect on the appearance of the magnetosomes (Fig. 5*B*). The dense packing of the antibodies on the magnetosomes indicated that a considerable amount of $MamA_{AMB-1}$ was located at the outermost layer of the magnetosomes. The dimension of magnetosomes significantly increased from 57.2 ± 7.8 nm (n = 25) to 72.7 ± 10.8 nm (n = 69) in height, and from 59.2 ± 7.6 nm (n = 25) to 90.7 ± 15.8 nm (n = 69) in width after labeling with anti-MamA antibody (Fig. 5 *C* and *D*). The height difference between labeled and nonlabeled magnetosomes (15 nm) was in good agreement with the diameter of the antibody (35).

A previous study has indicated that the recombinant His-MamA can attach to the MamA-eliminated magnetosomes prepared by the alkaline treatment (13). To elucidate the location of reconstructed His-MamA in the magnetosomes, immunolabeling was performed for both alkaline-treated and MamA-reconstructed magnetosomes. The anti-MamA antibody failed to bind to the alkaline-treated magnetosomes (Fig. 5*E*). This shows the depletion of $MamA_{AMB-1}$ from the magnetosomes by the treatment. After the reconstruction of the His-MamA to the alkaline-treated magnetosomes, antibodies densely bound to magnetosomes (Fig. 5*F*). The appearance of the immuno-labeled His-MamA-reconstructed magnetosomes was very similar to that

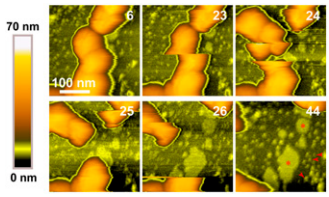

Fig. 3. Dissection of magnetosomes adsorbed on bare mica. The surface was scanned at 1.0 s/frame with the number of pixels of 256 × 256. This nanodissection treatment exposed the underlying sheet-like structure (asterisks). Also, small particles (which were measured ~3 nm in height) appeared on the mica surface (arrowheads). Numbers indicate frame number.

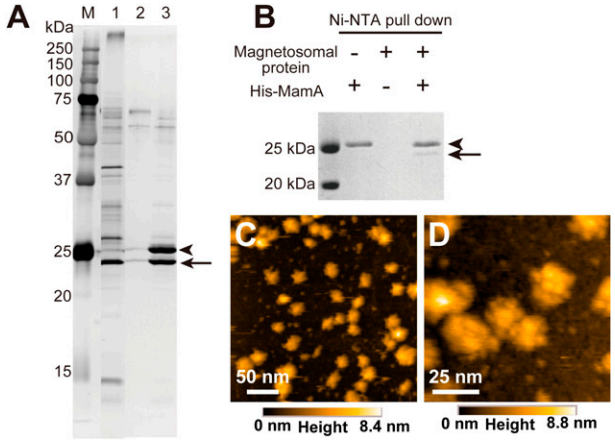

Fig. 4. Oligomerization of MamA. (*A*) SDS/PAGE analysis of binding magnetosomal proteins on the His-MamA affinity column. Protein bands were visualized by silver staining. Lane 1, solubilized magnetosome-associated proteins. Lane 2, eluted proteins from BSA column. Lane 3, eluted proteins from His-MamA affinity column. The 24-kDa protein (arrow) was identified as $MamA_{MS-1}$ by immunoblotting. Arrowhead shows that the His-MamA came off from the column. (*B*) Pull-down assays. $MamA_{MS-1}$ (arrow) was coprecipitated from solubilized magnetosome-associated proteins with His-MamA (arrowhead) binding to Ni-NTA resin. Gel was stained with Coomassie Brilliant Blue G-250. (*C*) AFM image of His-MamA oligomer on AP-mica. (*D*) High-magnification image of His-MamA oligomer on AP-mica. AFM images were recorded at an imaging rate of 1 s/frame; the number of pixels was 256 × 256.

of the untreated magnetosomes. This result suggests that the endogenous $MamA_{AMB-1}$ and the recombinant His-MamA share the binding site on the magnetosomes.

Effect of MamA Elimination on the Chain Structure. To examine the effect of MamA elimination on the chain structure of magnetosomes, spacing between magnetosome particles was compared between the intact magnetosomes and MamA-eliminated magnetosomes prepared by alkaline treatment (Fig. 6*A*). The averaged center-to-center distance between the adjacent particles in the intact magnetosomes (59.4 ± 6.2 nm, n = 364) was consistent with the spacing between magnetite crystals observed in cell using cryo-TEM (28). Interestingly, the averaged distance between the particles of alkaline-treated magnetosomes significantly increased (P < 0.0001, estimated using F test) by 3–4 nm (62.8 ± 7.8 nm, n = 336). On the other hand, the alkaline treatment had no significant effect on the distance between the magnetosomes purified from Δ*mamA* mutant (Fig. 6*B*). When the His-MamA was rebound to the alkaline-treated magnetosomes, the spacing between the magnetosome particles decreased (58.5 ± 5.8 nm [n = 172]) to the value consistent with that of the untreated magnetosomes (Fig. 6*A*). The interparticle spacings of the untreated magnetosomes and the MamA reconstructed magnetosomes showed no significant difference (P = 0.35, estimated using F test). These results indicate that MamA have an effect on the distance between magnetosomes.

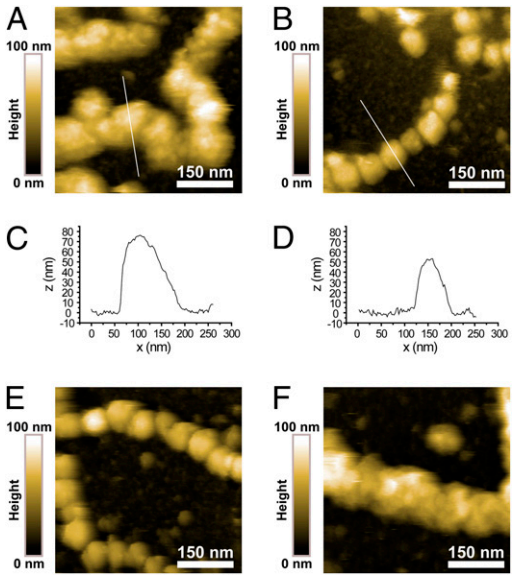

Fig. 5. AFM images of immuno-labeled magnetosomes. Magnetosomes labeled with (*A*) anti-MamA antibodies and (*B*) preimmuno serum. (*C* and *D*) Surface profile along the lines indicated in *A* and *B*. Magnetosomes labeled with anti-MamA antibodies after (*E*) alkaline treatment and (*F*) His-MamA reconstruction. AFM images were recorded at an imaging rate of 3 s/frame; number of pixels was (*A* and *B*) 200 × 200 and (*E* and *F*) 256 × 256.

Discussion

The aim of the present study is to characterize the structures and compositional organization of magnetosomes in an aqueous environment using AFM. The spatial localization, supramolecular organization, and functions of the individual components within the magnetosome must be determined to understand how this bacterial organelle functions as a magnetic compass. To date, AFM visualization of prokaryotic intramembrane structures at a spatial resolution close to 1 nm has been achieved for flat membranes such as purple membrane (36), chromatophore (25, 37), and outer membrane (38). It remains challenging, however, to obtain high-resolution images for a whole organelle that contains various molecular species and has a complex 3D structure. Here, we visualized the near-native hemispherical configuration of the isolated magnetosomes (Fig. 1). In the phase image, we were able to discern the surface structure at a lateral resolution of 4–8 nm, which should represent the molecular organization at the surface of the magnetosomes. Although this resolution is insufficient to determine the precise molecular organization, the lateral resolution obtained in this study is the best achieved so far for magnetosomal membrane in buffer condition.

The AFM showed that the magnetosome was ~61 nm in height. On the other hand, the crystal size of the magnetite was ~47 nm in diameter. Therefore, the thickness of the electron permeable organic layer was calculated to be 7 nm. Although magnetite crystal is enveloped by a lipid membrane, the thickness of the organic layer is significantly larger than single bilayer membrane. This means that the magnetic particle is surrounded by other organic components that may be composed of magnetosome-associated proteins. A previous TEM observation has identified the organic layer, termed the magnetosomal matrix (13). Based on the TEM observation, the magnetosomal matrix spread around the magnetosome vesicles several tens of nanometers in width. Instead of this huge structure, our AFM study revealed a thin organic layer. The possible reason for this difference is the variation in surface properties of the substrates or the imaging conditions between AFM and TEM.

The previous TEM observation has revealed also a fibrous texture that connects the flanking magnetosome particles (13). In the present AFM study, however, this structure was not observed in the magnetosome chains because of the difficulty of AFM to precisely trace deep features. To profile surface morphologies in narrow spaces, the AFM stylus must have both a high aspect ratio and a small apex radius. Otherwise, the apex of the AFM stylus cannot access the fine structures at the bottom of the trough. Although our AFM styli were sufficiently sharp to visualize the structure of the magnetosomes, an extremely high aspect ratio will be needed to define the interparticle connection.

As shown in Fig. 4 *C* and *D,* we were able to visualize His-MamA oligomers on the AP-mica, whereas small particles 3 nm

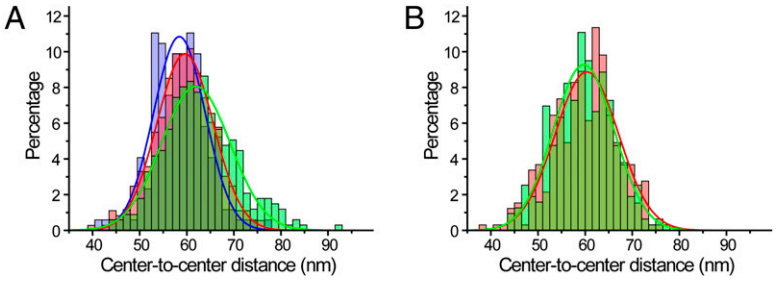

Fig. 6. Histogram of center-to-center distance between adjacent magnetosomes. (*A*) From wild type: intact; magenta, alkaline treated; green, MamA reconstructed; cyan. (*B*) From *ΔmamA* mutant: intact, magenta; alkaline-treated, green. Curves indicate fit to the Gaussian distributions.

in height instead of large complexes were observed on the bare mica (Fig. S4). This may be due to differences in the interaction between the proteins and substrates. In addition to the particles 3 nm in height, the particles 6–8 nm in height were also observed on the bare mica (Fig. 2*E*). These 6- to 8-nm particles are attributed to partially deoligomerized MamA complex, because they were not observed around the magnetosomes from *mamA* mutant (Fig. 2*G*). Moreover, these particles were not observed when the magnetosome was chemically fixed before depositing onto the bare mica. Therefore, the MamA proteins easily detached from magnetosomes in buffer conditions, indicating that MamA was loosely bound by the magnetosomes.

The most striking finding in this study was that the magnetosome vesicles were surrounded by MamA protein. The subcellular localization of MamA has been previously demonstrated. MamA-green fluorescent protein was observed to localize as a patchy line within the cell (3, 28). Also, immunogold staining with TEM showed that MamA associates with the magnetosomal matrix (13). In this study, the AFM imaging of the immunolabeled magnetosomes (Fig. 5) clearly indicated that MamA was located at the surface of the organelle. The close packing of the anti-MamA antibodies on the magnetosomes indicated that MamA protein densely covers the entire outer surface of the magnetosome chain. As described above, the thickness of the organic layer covering the magnetite is 7 nm. This value approximately coincides with the sum of the thickness of the bilayer lipid membrane and the height of the MamA oligomer. This finding supports the view that the magnetosome membrane vesicle is coated with MamA oligomers. Although we attempted to visualize MamA complexes on the surface of magnetosomes using bare mica and AP-mica as the substrates, we could not identify individual MamA oligomers on the magnetosome. This is likely due to the texture of the magnetosome surface, which is amorphous and closely packed with various types of protein.

The TPR protein MamA most probably functions as a receptor that interacts with a partner protein in the magnetosome. Our results showed that MamA interacts with MamA itself to form oligomer (Fig. 4), and binds to the surface of magnetosomes (Fig. 5). In addition, MamA further interacts with unidentified proteins that were extracted from the magnetosomes (Fig. 4*A*). These results suggest that MamA oligomers are anchored on the magnetosome membrane through magnetosome membrane-associated proteins, and partially through lipids of the magnetosome membrane. Because MamA is abundant relative to other magnetosome-associated proteins, MamA oligomers would be sparsely bound by the anchor proteins in the organic layer.

A previous study on *ΔmamA* mutant showed that the cells produce regular number of magnetosome vesicles. However, not all these vesicles are functional for the production of magnetite. Based on these observations, Komeili et al. proposed that MamA is part of the magnetosome assembly and maintenance processes such as protein sorting or activation of the magnetosome vesicles in response to external signals (28). In this study, we presented that MamA is located at the outermost layer of magnetosomes. With this spatial configuration of MamA in the magnetosomes, it is possible that MamA act as a scaffold that links between the magnetosome vesicles and cytoplasmic factors that activate the magnetite formation. Although our study showed a possibility that MamA contributes to the stabilization of magnetosome chain (Fig. 6), it is unclear how this stabilizing effect associates with magnetosome formation processes in vivo. Further studies on molecular assembly and function of MamA would expand our understanding of magnetosome formation.

It is now clear that bacteria are highly organized, possessing cytoskeletons, internal compartments, and carefully positioned macromolecular machines. To understand how they are organized and express their function, it is essential to unveil the ultrastructures under near-native conditions. Here, we visualized one of the most complex bacterial organelles, the magnetosome, in near-native conditions. To this end, AFM-based techniques such as immuno-labeling and nanodissection procedures are powerful approaches, as evidenced in this study. Combined with the possibility to reveal surface structures with high lateral resolution, AFM will exploit this unique avenue for the investigation of the ultrastructures of prokaryotic organelles.

Materials and Methods

Microorganisms and Cultures. *M. magneticum* AMB-1 (ATCC 700264), *mamA* deletion mutant of AMB-1 (28), and *M. magnetotacticum* MS-1 (ATCC 31632) were cultured in a liquid media under an O_2 (1%)–N_2 (99%) atmosphere at 25 °C in the dark (39). *Escherichia coli* strain BL21(DE3) (Novagen), containing pET15b-mam22 (32), was used for overproduction of His-tagged MamA. *E. coli* was cultivated as described (13).

Purification of Recombinant His-MamA. His-MamA was purified as previously described (32). Purified His-MamA was subjected to gel filtration column chromatography (Sephacryl S-300, GE Healthcare). The apparent molecular mass was calculated using a Gel Filtration Calibration Kit (GE Healthcare) as a standard.

Magnetosome Preparation. Magnetosomes were purified as previously described (13) and used immediately or stored at 4 °C without freezing. Alkaline treatment of the purified magnetosomes with 0.1 M Caps–NaOH buffer (pH 11.0) was performed as described elsewhere (13). TEM observation of the purified magnetosomes was performed using a JEOL JEM 2000EX TEM operating at 120 kV in bright-field mode. For reconstruction with His-MamA, the alkaline treated magnetosomes (3 mg wet weight) were incubated with the His-MamA (20 μM) in 200 μL of 10 mM Tris·HCl (pH 8.0) at 25 °C for 16 h, and then centrifuged at 8,000 × *g* for 5 min. The pellets obtained were washed with 1 mL of 10 mM Tris·HCl buffer (pH 8.0) and centrifuged at 8,000 × *g* for 5 min. The supernatant containing the unbound His-tagged His-MamA was removed by aspiration and resuspended in 10 mM Tris·HCl buffer (pH 8.0). This washing step was repeated three times.

Atomic Force Microscopy. Imaging was performed with a laboratory-built high-speed AFM, an extensively improved version of the previously reported AFM (40, 41). The high-speed AFM was equipped with small cantilevers (k = 0.1–0.2 N/m, f = 800–1,200 kHz in water) and operated in tapping mode. A lock-in amplifier (SR844-RF, Stanford Research Systems) was used to detect the phase difference between the cantilever oscillation and the excitation signal. The AFM styli were grown on each cantilever by electron beam deposition. Freshly cleaved mica, AP-mica, and hydrophobilized mica were used as substrates. AP-mica was prepared by depositing 0.05% 3-aminopropyltriethoxysilane (Shin-Etsu Chemical) on freshly cleaved mica and left for 3 min. Hydrophobilization of mica was performed using a vapor deposition method, in which hexame-

thyldisilazane (Shin-Etsu Chemical) and the freshly cleaved mica were placed simultaneously in a sealed container and incubated at 60 °C for 30 min. The purified magnetosomes (OD_{600nm}= 7) were adsorbed on the substrates in 10 mM Tris·HCl (pH 8.0). After 3 min, the sample was rinsed with 10 mM Tris·HCl (pH 8.0). For chemical fixation, the sample was incubated with 1% glutaraldehyde for 3 min. For immuno-labeling of MamA in the purified magnetosomes, the magnetosomes were adsorbed on the hydrophobilized mica and then incubated with 1% BSA in PBS for 5 min. Subsequently, the sample was incubated with anti-MamA rabbit polyclonal antibodies or preimmuno serum as described (13). After rinsing with PBS two times for 1 min each, the specimens were chemically fixed with 1% glutaraldehyde for 3 min in PBS.

Identification of Mica Binding Protein. The magnetosome suspension (OD_{600nm} = 7) was loaded onto a bare mica (76 × 26 mm), which was fixed on slide glass with double-stick tape and then incubated for 3 min. After the mica was washed three times with 10 mM Tris·HCl (pH 8.0), the mica was sonicated with an ultrasonic oscillator (Branson model 450; 20 kHz 10 W) to remove bound magnetosomes from the mica. AFM confirmed that only a few magnetosomes were present on the mica surface, and a large amount of the globular particles and a small amount of sheet-like structures remained on the mica. The resulting mica was incubated with 2% SDS containing 10 mM Tris·HCl (pH 8.0). Based on AFM observation, most of the particles were removed from the mica surface by SDS treatment. The proteins extracted from the mica were analyzed by SDS/PAGE.

MamA-affinity Chromatography. To prepare His-MamA affinity resin, 1 mL of CNBr-activated Sepharose 4B (GE Healthcare) was coupled with the purified His-MamA (1.2 mg). The His-MamA resin column (0.5 × 4 cm) was equilibrated with 10 mM Tris·HCl (pH 8.0) containing 0.1% sucrose monocaprate (equilibration buffer). To solubilize magnetosome-associated proteins, the magnetosomes purified from *M. magnetotacticum* MS-1 (~0.6 g, wet weight) were incubated with 10 mL of 10 mM Tris·HCl (pH 8.0) containing 2% sucrose monocaprate at 4 °C for 16 h. The suspension was then centrifuged at 10,000 × *g* for 15 min at 4 °C. After the resultant supernatant was dialyzed against the equilibration buffer, the protein solution (12 mL) was subjected to the His-MamA-column with a flow rate of 1 mL/h. After that, the column was washed with the equilibration buffer containing 1 M NaCl. Then the binding proteins were eluted with 0.1 M Caps-NaOH buffer (pH 11.0) containing 0.1% sucrose monocaprate from the column.

Pull-Down Assay. The solution of the His-MamA (50 μL, 1 mg/mL) was mixed with 25 μL of the Ni-NTA resin (Qiagen), which had been equilibrated with the pull-down buffer (20 mM Tris·HCl [pH 8.0], 0.2 M NaCl, 5 mM imidazole). The Ni-NTA resin with His-MamA was incubated with 350 μL of the solubilized magnetosome-associated proteins from *M. magnetotacticum* MS-1 (0.14 mg/mL), in pull-down buffer at 25 °C for 1 h. After the resin was washed three times with 1 mL of the washing buffer (20 mM Tris·HCl, pH 8.0, 0.2 M NaCl, 60 mM imidazole), the binding protein was eluted from the resin with 30 μL of elution buffer (20 mM Tris·HCl, pH 8.0, 0.2 M NaCl, 250 mM imidazole) and analyzed by SDS/PAGE.

Physical and Chemical Measurements. The protein contents were determined using the bicinchoninic acid method (BCA Protein Assay Kit, Pierce Chemical) with BSA as a standard. SDS/PAGE was performed according to the method of Laemmli (42). Immunoblotting analysis was performed as described elsewhere (13).

ACKNOWLEDGMENTS. We thank A. Komeili (University of California, Berkeley, CA) for providing the *mamA* deletion mutant of *M. magneticum* AMB-1.

1. Bazylinski D-A, Frankel R-B (2004) Magnetosome formation in prokaryotes. *Nat Rev Microbiol* 2:217–230.
2. Schüler D (2008) Genetics and cell biology of magnetosome formation in magnetotactic bacteria. *FEMS Microbiol Rev* 32:654–672.
3. Komeili A (2007) Molecular mechanisms of magnetosome formation. *Annu Rev Biochem* 76:351–366.
4. Faivre D, Schüler D (2008) Magnetotactic bacteria and magnetosomes. *Chem Rev* 108: 4875–4898.
5. Matsunaga T, et al. (2005) Complete genome sequence of the facultative anaerobic magnetotactic bacterium *Magnetospirillum* sp. strain AMB-1. *DNA Res* 12:157–166.
6. Grünberg K, et al. (2004) Biochemical and proteomic analysis of the magnetosome membrane in *Magnetospirillum gryphiswaldense*. *Appl Environ Microbiol* 70:1040–1050.
7. Matsunaga T, Okamura Y (2003) Genes and proteins involved in bacterial magnetic particle formation. *Trends Microbiol* 11:536–541.
8. Schübbe S, et al. (2003) Characterization of a spontaneous nonmagnetic mutant of *Magnetospirillum gryphiswaldense* reveals a large deletion comprising a putative magnetosome island. *J Bacteriol* 185:5779–5790.
9. Ullrich S, Kube M, Schübbe S, Reinhardt R, Schüler D (2005) A hypervariable 130-kilobase genomic region of *Magnetospirillum gryphiswaldense* comprises a magnetosome island which undergoes frequent rearrangements during stationary growth. *J Bacteriol* 187: 7176–7184.
10. Bazylinski D-A, Schübbe S (2007) Controlled biomineralization by and applications of magnetotactic bacteria. *Advances in Applied Microbiology*, eds Laskin AI, Sariaslani S, Gadd GM (Academic, London), pp 21–62.
11. Richter M, et al. (2007) Comparative genome analysis of four magnetotactic bacteria reveals a complex set of group-specific genes implicated in magnetosome biomineralization and function. *J Bacteriol* 189:4899–4910.
12. Martins J-L, Keim C-N, Farina M, Kachar B, Lins U (2007) Deep-etching electron microscopy of cells of *Magnetospirillum magnetotacticum*: Evidence for filamentous structures connecting the magnetosome chain to the cell surface. *Curr Microbiol* 54:1–4.
13. Taoka A, et al. (2006) Spatial localizations of Mam22 and Mam12 in the magnetosomes of *Magnetospirillum magnetotacticum*. *J Bacteriol* 188:3805–3812.
14. Scheffel A, et al. (2006) An acidic protein aligns magnetosomes along a filamentous structure in magnetotactic bacteria. *Nature* 440:110–114.
15. Komeili A, Li Z, Newman D-K, Jensen G-J (2006) Magnetosomes are cell membrane invaginations organized by the actin-like protein MamK. *Science* 311:242–245.
16. Gorby Y-A, Beveridge T-J, Blakemore RP (1988) Characterization of the bacterial magnetosome membrane. *J Bacteriol* 170:834–841.
17. Lins U, Farina M, Kachar B (2003) Membrane vesicles in magnetotactic bacteria. *Microbiol Res* 158:317–320.
18. Taoka A, Asada R, Wu L-F, Fukumori Y (2007) Polymerization of the actin-like protein MamK, which is associated with magnetosomes. *J Bacteriol* 189:8737–8740.
19. Pradel N, Santini C-L, Bernadac A, Fukumori Y, Wu L-F (2006) Biogenesis of actin-like bacterial cytoskeletal filaments destined for positioning prokaryotic magnetic organelles. *Proc Natl Acad Sci USA* 103:17485–17489.
20. Frankel R-B, Bazylinski D-A (2006) How magnetotactic bacteria make magnetosomes queue up. *Trends Microbiol* 14:329–331.
21. Koster A-J, et al. (1997) Perspectives of molecular and cellular electron tomography. *J Struct Biol* 120:276–308.
22. Dufrêne Y-F (2008) Towards nanomicrobiology using atomic force microscopy. *Nat Rev Microbiol* 6:674–680.
23. Dufrêne Y-F (2004) Using nanotechniques to explore microbial surfaces. *Nat Rev Microbiol* 2:451–460.
24. Engel A, Müller D-J (2000) Observing single biomolecules at work with the atomic force microscope. *Nat Struct Biol* 7:715–718.
25. Bahatyrova S, et al. (2004) The native architecture of a photosynthetic membrane. *Nature* 430:1058–1062.
26. Fotiadis D, et al. (2003) Atomic-force microscopy: Rhodopsin dimers in native disc membranes. *Nature* 421:127–128.
27. García R, Magerle R, Perez R (2007) Nanoscale compositional mapping with gentle forces. *Nat Mater* 6:405–411.
28. Komeili A, Vali H, Beveridge T-J, Newman D-K (2004) Magnetosome vesicles are present before magnetite formation, and MamA is required for their activation. *Proc Natl Acad Sci USA* 101:3839–3844.
29. Hansma H-G, et al. (1992) Reproducible imaging and dissection of plasmid DNA under liquid with the atomic force microscope. *Science* 256:1180–1184.
30. Hoh J-H, Sosinsky G-E, Revel J-P, Hansma P-K (1993) Structure of the extracellular surface of the gap junction by atomic force microscopy. *Biophys J* 65:149–163.
31. Mitra K, Ubarretxena-Belandia I, Taguchi T, Warren G, Engelman D-M (2004) Modulation of the bilayer thickness of exocytic pathway membranes by membrane proteins rather than cholesterol. *Proc Natl Acad Sci USA* 101:4083–4088.
32. Okuda Y, Fukumori Y (2001) Expression and characterization of a magnetosome-associated protein, TPR-containing MAM22, in *Escherichia coli*. *FEBS Lett* 491:169–173.
33. Okuda Y, Denda K, Fukumori Y (1996) Cloning and sequencing of a gene encoding a new member of the tetratricopeptide protein family from magnetosomes of *Magnetospirillum magnetotacticum*. *Gene* 171:99–102.
34. D'Andrea L-D, Regan L (2003) TPR proteins: The versatile helix. *Trends Biochem Sci* 28: 655–662.
35. Kienberger F, Mueller H, Pastushenko V, Hinterdorfer P (2004) Following single antibody binding to purple membranes in real time. *EMBO Rep* 5:579–583.
36. Müller D-J, Schabert F-A, Büldt G, Engel A (1995) Imaging purple membranes in aqueous solutions at sub-nanometer resolution by atomic force microscopy. *Biophys J* 68:1681–1686.
37. Scheuring S, et al. (2003) Nanodissection and high-resolution imaging of the *Rhodopseudomonas viridis* photosynthetic core complex in native membranes by AFM. Atomic force microscopy. *Proc Natl Acad Sci USA* 100:1690–1693.
38. Jarosławski S, Duquesne K, Sturgis J-N, Scheuring S (2009) High-resolution architecture of the outer membrane of the Gram-negative bacteria *Roseobacter denitrificans*. *Mol Microbiol* 74:1211–1222.
39. Blakemore R-P, Maratea D, Wolfe R-S (1979) Isolation and pure culture of a freshwater magnetic spirillum in chemically defined medium. *J Bacteriol* 140:720–729.
40. Ando T, et al. (2001) A high-speed atomic force microscope for studying biological macromolecules. *Proc Natl Acad Sci USA* 98:12468–12472.
41. Ando T, Uchihashi T, Fukuma T (2008) High-speed atomic force microscopy for nano-visualization of dynamic biomolecular processes. *Prog Surf Sci* 83:337–437.
42. Laemmli U-K (1970) Cleavage of structural proteins during the assembly of the head of bacteriophage T4. *Nature* 227:680–685.